Simulation of injector dynamics during Steady Inductive Helicity Injection current drive in the Helicity Injected Torus experiment

Chris Hansen,[1,2,*] George Marklin,[1] Brian Victor,[3] Cihan Akcay,[4] and Thomas Jarboe[3,1]

[1] *PSI-Center, University of Washington, Seattle, Washington 98195, USA*

[2] *Columbia University, New York, New York 10027, USA*

[3] *HIT-SI Group, University of Washington, Seattle, Washington 98195, USA*

[4] *Los Alamos National Laboratory, Los Alamos, New Mexico 87545, USA*

(Dated: April 27, 2015)

Abstract

We present simulations of inductive helicity injection in the Helicity Injected Torus with Steady Inductive helicity injection (HIT-SI) device that treat the entire plasma volume in a single dynamic MHD model. A new fully 3D numerical tool, the PSI-TET code, was developed that provides the geometric flexibility required for this investigation. Implementation of a zero-β Hall MHD model using PSI-TET will be presented including formulation of a new self-consistent magnetic boundary condition for the wall of the HIT-SI device. Results from simulations of HIT-SI are presented focusing on injector dynamics that are investigated numerically for the first time. Asymmetries in the plasma loading between the two helicity injectors and progression of field reversal in each injector are observed. Analysis indicates cross-coupling between injectors through confinement volume structures. Injector impedance is found to scale with toroidal current at fixed density, consistent with experimental observation. Comparison to experimental data with an injector drive frequency of 14.5 kHz shows good agreement with magnetic diagnostics. Global mode structures from Bi-Orthogonal decomposition agree well with experimental data for the first four modes.

* hansec@uw.edu

I. INTRODUCTION

The development of efficient, steady state current drive is a crucial issue for many magnetic confinement fusion concepts[1, 2]. The Helicity Injected Torus-Steady Inductive (HIT-SI) experiment[3, 4] studies the use of Steady Inductive Helicity Injection (SIHI) current drive as a means for sustaining plasma current in closed toroidal geometries. Although all current drive methods can be cast in terms of helicity and its injection, the term "helicity injection current drive" is usually ascribed to a class of methods where helicity is injected in an experimentally convenient way with plasma dynamo[5–8] and other dynamic processes[9] used to distribute the current driving force where it is needed. Many experiments have successfully applied this method using axisymmetric injection fields, such as Coaxial Helicity Injection (CHI) on spheromaks[10–12] and spherical tori[13, 14] and Oscillating Field Current Drive (OFCD)[15] on Reverse Field Pinches (RFPs).

The necessary involvement of plasma dynamics in these current drive methods complicates their understanding. This motivates the use of numerical models to analyze the physical phenomenon involved. Single fluid MHD and Hall-MHD models have been used previously to study helicity injection in SSPX[16, 17], NSTX[18], Pegasus[19] and other experiments[20, 21]. These investigations have helped elucidate relaxation and other processes that reproduce many of the qualitative features observed in experimental data. In order to gain confidence in understanding derived from these models, direct comparison must be made between observations and simulation results. This process of validating[22–24] MHD as an appropriate and predictive model for existing and future magnetic confinement experiments is an area of significant activity[25, 26].

The SIHI current drive method investigated on the HIT-SI experiment differs from previously studied helicity injection methods through the use of non-axisymmetric applied fields. Additionally, these fields are generated inductively by circuits on injectors external to the primary confinement volume. Detailed descriptions of the experiment and its operation are available in references [27] and [28]. Figure 1 shows a cut-away of the experiment (colors indicate segments that are electrically isolated from one another). Helicity is injected into the plasma by oscillating two sets of coils, the flux and voltage coil, on each of two semi-toroidal injectors attached to either side of the nominally axisymmetric bow-tie flux conserver. These coils produce helical magnetic fields that link through the injector and flux

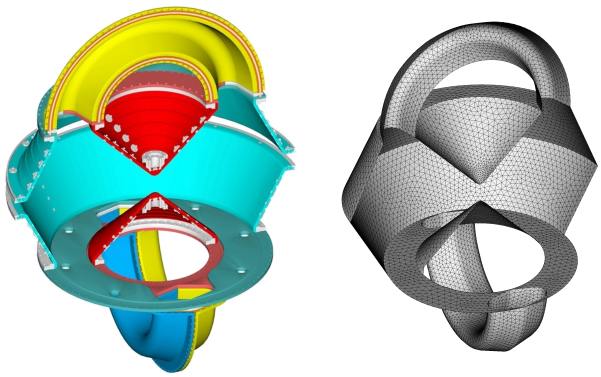

(a)Machine Geometry (b)Simulation Domain

FIG. 1. Cut-away view of the HIT-SI experiment and simulation domain. Only the boundary of the computational grid is shown for comparison with the source CAD representation.

conserver volumes, which both generate[4] and sustain[8] a spheromak[29, 30] equilibrium. A more detailed description of the operation will be provided in section III as part of the discussion of boundary conditions used in simulations.

SIHI has shown significant promise, producing the first sustained spheromaks with observed pressure confinement[31] while removing electrode surfaces – a significant source of impurity production. Previous numerical studies of this method by Izzo[32] and Akcay[26] have advanced the understanding of SIHI current drive in HIT-SI. However, these studies simplified the plasma geometry, by removing the helicity injectors, so that the remaining plasma region is axisymmetric. Injection fields in the confinement volume were then produced by applying magnetic field boundary conditions to mimic the effect of the injector circuits. These changes allowed the widely used and verified NIMROD code[33, 34] to be applied to HIT-SI, but removed plasma dynamics internal to the injectors from the simulations.

In this paper we present the first simulations of HIT-SI that treat the full plasma volume in a single coupled simulation. These simulations are found to agree well with experimental data and previous simulations by Akcay[26]. By including the injector regions, agreement is improved between the injector impedance observed in simulations. Field reversal in the injectors, due to AC operation of the driving circuits, is observed to progress asymmetrically relative to the injector mouths once a significant toroidal current forms. Circuit loading, produced by plasma response, is found to be more dissipative in one injector than another, where the "dominant" injector is dependent on relative phasing. Analysis of injector coupling

to plasma eigenmodes indicates cross-coupling through intermediary modes may play a role in determining this asymmetry. Simulations were enabled by the development of a new MHD code (PSI-TET) that is capable of representing complex 3D geometry easily.

The remainder of this paper will be organized as follows: In section II the PSI-TET code[35] will be briefly described, focusing on the features that enabled the simulations to follow. In section III the numerical model (zero-β MHD) will be presented along with details of its implementation using vector finite elements. A new boundary condition is also presented that self-consistently models the insulator coated conducting wall and driving circuits of HIT-SI. Section IV will present results of simulations performed with the zero-β model focusing on new physical phenomena associated with modeling the injectors. Comparison to experimental data from magnetic diagnostics will be presented in V.

II. PSI-TET

The PSI-center TETrahedral mesh (PSI-TET) code is a 3D high order finite element framework that supports the development of multi-physics models on unstructured tetrahedral grids. This discretization enables the representation of complex 3D geometries easily, such as the HIT-SI experiment. An interface to the CUBIT[36] and T3D[37] meshing softwares allow generation of computational grids directly from Computer-Aided Design (CAD) models – accurately representing experimental geometries. High order finite element representations are provided in the form of nodal scalar (Lagrange) and Curl-Conforming vector (Nedelec[38, 39]) basis sets, with support to add additional sets as desired. PSI-TET is a massively parallel code supporting both distributed (task) and shared (thread) memory parallelization using a MPI+OpenMP model[40, 41]. To enable the use of large meshes and efficiently utilize parallel computing environments the physical domain is decomposed using the METIS[42] partitioning library. Linear algebra operations are supported through either a native implementation or an interface to the PETSc library[43]. This allows the user to design code that can access a wide variety of solvers through a common and consistent interface.

A main feature of the PSI-TET framework is built-in mechanics and support for constructing preconditioners using the geometric multi-grid method[44–47]. A base grid is imported and successively refined, by subdividing each edge in the mesh, resulting in a hierarchy of

progressively finer grids. Multi-grid levels are defined by creating a linear discretization for each of the coarse grids and additional levels for each polynomial order up to the maximum desired order on the finest grid. New nodes generated during grid refinement are adjusted to the CAD boundary using the CUBIT or T3D interfaces. Quadratic or cubic mappings from logical to physical space can also be constructed to accurately capture boundary curvature when using high order representations using the same interface.

III. NUMERICAL MODEL

For this investigation a zero-β Hall-MHD model was implemented in PSI-TET. This model simplifies the Hall-MHD equations for a fully ionized, quasi-neutral ($n_i = n_e = n$) plasma by assuming temperature and density are both uniform in space and constant in time. This reduces the system of equations to the plasma momentum (eq. 1a) and induction (eq. 1b) equations. The current density is derived from the magnetic field through a low frequency approximation to Ampere's law (eq. 1c). The electric field is given by generalized Ohm's law (eq. 1d) including resistive, Hall and electron inertia terms. The fluid stress tensor is approximated with a simplified kinematic viscosity, $\Pi = -\nu\nabla\mathbf{u}$. The remaining constants are plasma density (n), resistivity (η), ion mass (m_i), enhanced electron mass (m_e^*) and charge constant (e).

$$nm_i\left[\frac{\partial\mathbf{u}}{\partial t} + \mathbf{u}\cdot\nabla\mathbf{u}\right] = \mathbf{J}\times\mathbf{B} - \nabla\cdot\Pi \tag{1a}$$

$$\frac{\partial\mathbf{B}}{\partial t} = -\nabla\times\mathbf{E} \tag{1b}$$

$$\mathbf{J} = \frac{1}{\mu_0}\nabla\times\mathbf{B} \tag{1c}$$

$$\mathbf{E} = -\mathbf{u}\times\mathbf{B} + \eta\mathbf{J} + \frac{1}{ne}\left(\mathbf{J}\times\mathbf{B} + \frac{m_e^*}{e}\frac{\partial\mathbf{J}}{\partial t}\right) \tag{1d}$$

This model was chosen based on existing numerical studies[26] where it was shown to be a suitable starting case for modeling HIT-SI. Two-fluid effects, included through the Hall term in Ohm's law, are expected to be important in HIT-SI as the ion inertial scale ($d_i \approx 8$ cm) is comparable to experimental length scales, such as the injector diameter ($l_{inj} = 14$ cm),

for the simulations presented in section IV. The importance of these effects have also been confirmed empirically as simulations using a resistive MHD model were unable to capture the rapid formation observed in experimental data[26]. The inertia term in Ohm's law is included for numerical convenience and used in conjunction with an enhanced electron mass to artificially damp Whistler waves with high spatial and temporal frequency– reducing the stiffness of the numerical system. An enhancement factor of 100, yielding a mass ratio of $\frac{m_i}{m_e^*} \approx 36$ for a Deuterium plasma, was found to increase solver speed without affecting plasma dynamics[26].

A. Implementation

Equations 1a and 1b are implemented in PSI-TET using the Crank-Nicolson centered, implicit method for time advance. The resulting non-linear system of equations are discretized in weak form using a Galerkin finite element approach on an unstructured tetrahedral grid. The magnetic field is expressed using a vector element representation, which defines the solenoidal and longitudinal components of the vector field on distinct subsets of the basis set. This defines a natural Helmholtz-like decomposition (eq. 2) within the representation, enabling boundary conditions that treat the two subspaces separately – as with the SIHI boundary condition described below.

$$\mathbf{B} = \nabla \times \mathbf{A} + \nabla\phi \tag{2}$$

Basis functions are defined using the hierarchical set of Schöberl[39]. Plasma velocity is discretized using a scalar Lagrange basis for each Cartesian component of the vector field. Both representations support variable polynomial degree, and representations up to 4th order are currently available. For the work presented here, quadratic basis sets were used for both the magnetic field and plasma velocity. Vector elements have been used extensively in electrodynamic modeling[48, 49] and have also been applied to incompressible MHD[50, 51], where both the vector potential and fluid vorticity are represented using the same basis. However, to the authors' knowledge this is the first application of vector finite elements to representation of the magnetic field directly in MHD.

The discretized non-linear system of equations is solved using Newton iteration with the preconditioned Generalized Minimum RESidual (GMRES) method[52] used to provide an

approximate inverse for the system Jacobian. Preconditioning is performed using geometric multi-grid with a V-cycle iteration, where coarse representations are defined by first reducing the polynomial order of the representation and then coarsening the underlying tetrahedral mesh – as described above. Smoothing on each level is performed by a few GMRES iterations that are further preconditioned by a block-Jacobi method – with local direct solves (LU)[53]. For the simulations presented in this paper this method provided a significant speed improvement over single-level preconditioners such as additive-Schwarz, block-Jacobi and incomplete factorizations.

B. SIHI Boundary Conditions

Boundary conditions for SIHI current drive in HIT-SI have posed a challenge for numerical models. The device is constructed out of 1/2" thick copper to provide a good flux conserver. The plasma facing surface is then coated with a thin insulating layer in order to ensure purely inductive operation of the injectors. As no external magnetic field is initially applied this enforces that both the magnetic flux and current density normal to the boundary must be zero (eq. 3). By restricting current flow to the boundary magnetic flux and injected power are able to redistribute over the boundary in response to plasma dynamics. Capturing this effect is expected to be important in accurately modeling SIHI current drive.

$$\mathbf{B} \cdot \hat{\mathbf{n}} = \mathbf{J} \cdot \hat{\mathbf{n}} = 0 \tag{3}$$

The constraint on the magnetic flux is satisfied with a perfectly conducting wall boundary condition. However, the constraint on current density is more complicated as it amounts to restriction of the functional form of the tangential magnetic field on the boundary, given by equation 4 where the subscript t denotes vector components tangential to the boundary.

$$(\nabla \times \mathbf{B}) \cdot \hat{\mathbf{n}} = 0 \rightarrow \mathbf{B}_t = \nabla_t \chi \tag{4}$$

In previous simulations using an axisymmetric boundary this effect is modeled by a thin boundary layer with high resistivity relative to the plasma value. High resistivity impedes current flow across this layer – approximating the insulating coating. To prevent numerical issues associated with this sharp variation in resistivity, it is necessary to introduce a matching boundary layer in the mesh so that the variation can occur within a single cell.

Generating such a mesh is straightforward for a 2D poloidal mesh. However, this method proved impractical for a tetrahedral mesh of HIT-SI due to the complex geometry where the injectors meet the confinement volume. In order to avoid this requirement a new boundary condition has been developed to restrict $J \cdot \hat{n}$ at the wall directly, by leveraging the subspace decomposition provided by the vector elements used to represent the magnetic field. The requirement that tangential magnetic field on the boundary must be curl-free (eq. 4) can be straightforwardly enforced using the vector element representation. A Dirichlet boundary condition is applied to the solenoidal subspace only, reducing the tangential field to the gradient of a scalar potential on the boundary.

This boundary condition also provides a simple way to apply driving fields to the injectors. By allowing the boundary potential to be multi-valued, jumps can be applied to enforce the loop integral of the magnetic field, $\oint \mathbf{B} \cdot \mathbf{dl} = f(t)$, on each topologically distinct closed path on the boundary. By virtue of Ampere's law this is equivalent to specifying the current passing through any surface enclosed by the given path. For HIT-SI, two unique paths exist for each injector and correspond to current passing through the injector handle, in the plasma, and current passing between the injector and the confinement volume, outside the plasma. Experimentally these currents correspond to the measured injector current, driven by the voltage coil, and total current in all windings of the flux coil respectively. The driving circuits on HIT-SI are then modeled using these jump conditions to reproduce the experimentally observed injector flux and current waveforms.

C. Flux Waveform Feedback

For HIT-SI simulations, the external drive circuits and their coupling to the plasma are not simulated directly. As a result, boundary conditions are used to reproduce the experimentally observed plasma quantities of flux and current in each injector. Current is controlled directly by the relevant boundary condition. Injector flux on the other hand is related to the boundary condition on flux coil current through plasma dynamics in the injector. In order to reproduce the desired flux waveform, the amplitude of the effective flux coil currents are adjusted in time based on the actual injector flux. A Proportional-Integral-Differential (PID) control algorithm is used to set the flux coil current in each injector from the measured injector fluxes at the beginning of each time step. An example of the

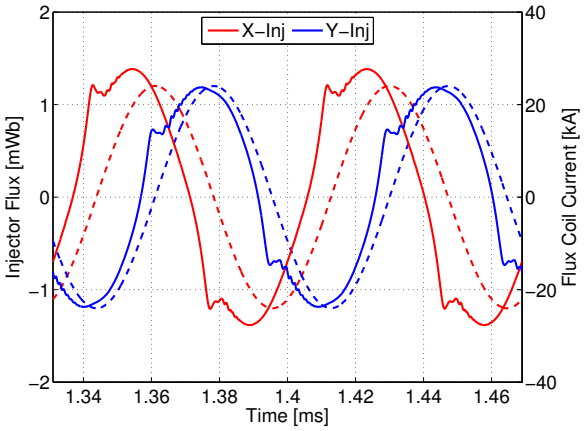

FIG. 2. Injector flux (dashed) and flux coil current (solid) waveforms from the PSI-TET baseline simulation near toroidal current saturation. Higher coil current and a larger phase offset (at zero crossing) are required for the X-injector to drive the desired flux waveform, when compared to the Y-injector.

injector flux coil currents required to produce sinusoidal flux waveforms during the baseline simulation presented in section in section IV is shown in figure 2. The required coil current waveform deviates significantly from the flux waveform in both phase and shape, indicating variation in the equivalent circuit inductance and resistivity throughout an injector cycle. The observed coil current waveforms from simulation are in qualitative agreement with experimental observations, which show similar structures and contain the same asymmetry between the X and Y injectors – indicating a difference in circuit loading between the two injectors. Details of this asymmetry and the waveform shape will be discussed further in the following section in reference to related plasma activity.

IV. RESULTS

In this section we present the results, focusing on injector dynamics, from initial simulations of the HIT-SI experiment using the model presented above. A benchmark simulation was performed for direct comparison to experimental data (presented in the next section) along with supplemental simulations to investigate injector physics, by varying parameters around the base case. The benchmark case was performed with physical parameters set to closely match experimentally observed values, shown in table I, for experimental shot

122385. This shot was chosen as it has been extensively studied both experimentally[8, 28] and numerically[26]. This shot does not constitute the highest performance achieved in HIT-SI, but is representative of operation in this regime.

The flux and current waveforms in each injector were driven sinusoidally as $\sin(2\pi f_{inj} t + \phi_0^i)$ with a linear ramp in amplitude to the steady state values shown in table I applied over the first injector period (69 μs). The starting phase (ϕ_0^i) was set independently for each waveform to match the relative phase offsets experimentally imposed during 14.5 kHz operation in HIT-SI. A starting phase of 0 and $-\pi/2$ was used for the X and Y injector currents respectively, with the related flux waveform on each injector set to lead the current waveform by 1 μs.

Density is measured in the experiment using a single interferometry chord. A steady increase in density is observed throughout the shot along with oscillations at the injector frequency, see figure 7 in reference [8]. For these simulations a density consistent with the averaged density immediately following formation of toroidal current was chosen, as in previous studies[26]. The experimental temperature range is based on measurements using a Langmuir probe. Experimental resistivity and viscosity are derived from the density and temperature measurements using the Spitzer[54] model for resistivity ($\eta = 0.51 n e^2 \tau_e / m_e$) and the Braginskii[55] model for parallel viscosity ($\nu = 0.96 n k T_i \tau_i$). Resistivity for the base simulation was chosen in order to match the toroidal current between the simulation and experiment during flattop. Resistivities for additional simulations presented in section IV C are shown in parentheses.

The computational mesh was constructed using T3D[37] and a simplified CAD representation of the HIT-SI device where the diagnostic gap on the outboard midplane has been removed. The resulting simulated plasma volume, shown in figure 1(b), captures the full experimental plasma domain well, shown in figure 1(a). The same computational grid was used for all simulations and consists of a base grid with a single mesh refinement resulting in an average edge length of 2.1 cm for the solution grid. The average node spacing is $h \approx 1$ cm for the quadratic basis functions used for discretization. Slightly higher resolution exists near the nose cone and injector mouths due to small geometric features in these areas. Convergence was checked by performing partial simulations (500 μs in length) with higher polynomial degree (cubic) on the same grid and higher grid resolution with the same polynomial degree ($h \approx 0.5$ cm). The time step was dynamically varied as the simulation

TABLE I. Run parameters for the HIT-SI baseline simulation in comparison to experimental values from shot 122385.

Parameter	Experiment	Simulation
Injector Current [kA]	10-20	21
Injector Flux [mWb]	0.6-1.4	1.2
f_{inj} [kHz]	14.5	14.5
n_e [m^{-3}]	$1 - 4 \times 10^{19}$	1.5×10^{19}
T_e [eV]	6-12	8
η/μ_0 [m^2/s]	25-9	16 (12.5, 25)
ν/ρ [m^2/s]	200-1000	260

advanced to maintain a constant number of linear iterations per time step. A maximum time step of 60 ns was imposed, determined by convergence studies. Decreases in the time step were only seen during injector reversal periods, resulting in an average time step very close to the 60 ns maximum.

A. Injector Coupling to the Confinement Volume

By including the injectors in the simulation domain, connection of the injector fields to the magnetic object in the confinement volume can be analyzed. HIT-SI operation can be divided into two time periods based on the amplitude of toroidal current present in the confinement volume. Before formation of a strong toroidal current the confinement volume is dominated by an object with primarily odd symmetry, which closely matches the symmetry of the applied field from a given injector. Figure 3 shows the magnetic field structure from the baseline simulation in the X-Z plane during this period. The plot is at a time in the simulation when the visible injector (X-Injector) has peak flux and current. The full magnetic structure is mostly $n = 1$ symmetric with injector magnetic field linking into an aligned structure in the confinement volume. The magnetic configuration in the confinement volume closely matches a linear combination of the 2nd and 3rd force-free eigenstates of the domain[35]– solutions to the eigenvalue equation $\mu_0 \mathbf{J} = \lambda \mathbf{B}$. The applied

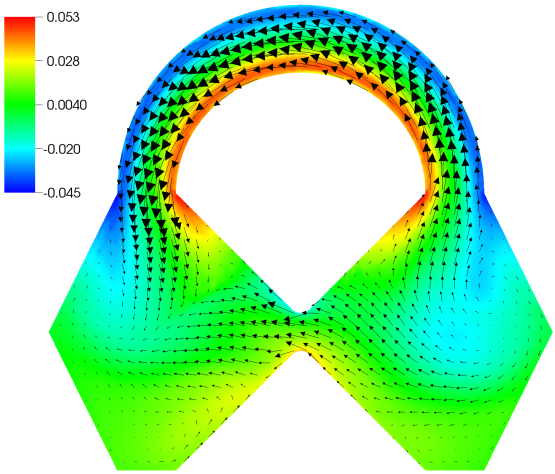

FIG. 3. Magnetic field in the X-Z plane from a PSI-TET simulation before formation of a toroidal current (0.087 ms). In-plane field is shown as the black vectors while out-of-plane field strength is indicated by the shaded cross-section (scale in [T]). The X-Injector and confinement volume are visible.

injector fields directly couple to these states, see section IV B. During the pre-formation phase this structure grows and rotates in time to align itself with the dominant injector, consistent with observations of $n = 1$ mode activity in experimental data, simulations[26] and Taylor theory approximation[4, 56].

The configuration produced early in time is ideally unstable[57, 58] and relaxes[9] once it reaches sufficient free energy to the desired spheromak equilibrium that is primarily axisymmetric. In this post-formation phase, a different coupling of the injectors to the confinement volume is observed. As the spheromak energy is increased the injector fields are forced to align with this object by virtue of reconnection, producing a new state during peaks of injector flux and current, shown in figure 4. At this time the spheromak object is clearly visible as a large $n = 0$ structure in the out of plane component of the magnetic field. Flux from the injector is forced to align with the spheromak as it exits the injector, causing the driven current channel to "lean" against the inner and outer walls of the flux conserver. This configuration, which was expected during design of HIT-SI[3] and observed internal to the confinement volume in previous simulations, is expected to be conducive to current drive in the spheromak[8] – by maintaining parallel current in the edge of the plasma. As the main

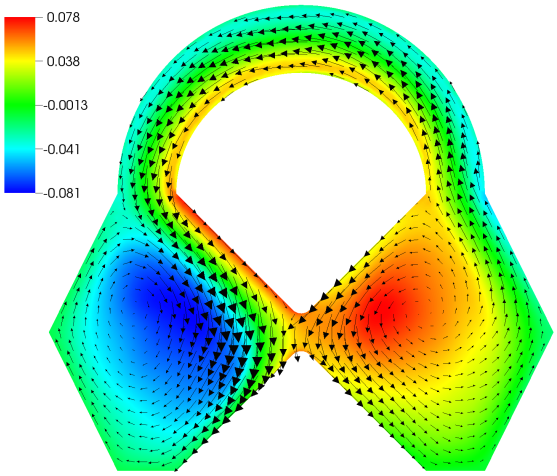

FIG. 4. Magnetic field in the X-Z plane from a PSI-TET simulation following formation of a toroidal current (1.4 ms). In-plane field is shown as the black vectors while out-of-plane field strength is indicated by the shaded cross-section (scale in [T]).

magnetic structure is now largely symmetric it does not rotate, but instead "tips" back and forth as the injector channels reconnect during reversal of the injector to align with the spheromak on the opposite side. Coupling to the confinement volume also begins to effect the field structure inside the injectors seen as an $n = 0$ variation in the amplitude of the out of plane field strength in figure 4. As the current ratio ($\frac{I_\phi}{I_{inj}}$) increases, this effect becomes more pronounced and the flux profile across the injector mouth can vary significantly from its pre-formation profile.

B. Injector Dynamics

The plasma region inside the injectors introduces a rich set of dynamics that has not been well studied previously. In fact, the injectors introduce new, numerically challenging regions due to dynamics associated with field reversal. The boundary conditions driving the injectors always push field in from the boundary, resulting in reversal that occurs by injecting magnetic flux and current in the opposite direction of existing fields. As new flux is injected, the existing flux is compressed into a progressively smaller channel in the center of the injector. When the current gradients associated with this flux transition become large

enough they drive instability at the interface, breaking the boundary into islands, and field within the channel reverses to match the direction of the incoming flux. Throughout this process, incoming flux near the wall remains well behaved due to the nearby conducting surface. Figure 5 shows an example of the magnetic field structure midway through the reversal process in the X-injector. At this time, the flux channel has broken up into islands and field is reversing so that the field flows uniformly from right to left through the injector. The primary reversal phase, characterized by fluctuations and islands, spans less than 4 μs in the baseline simulation, making it much faster than other non-linear phenomena present in the confinement volume. This time scale is consistent with the Sweet-Parker[59, 60] reconnection timescale, $\tau_{sp} = \sqrt{\tau_A \tau_{L/R}} \approx 3.2$ μs, computed for current sheets in the injector just before the onset of macroscopic reversal (344 μs). At this time the injector flux reverses on a scale of $\approx$ 4 cm with average field strength in the reversal channel of $\approx$ 30 mT. Reconnection layers associated with reversal are not fully resolved[61] in these simulations so only macroscopic dynamics will be discussed here.

Reversal within a single injector progresses asymmetrically with respect to the injector mouths, as seen in figure 5. Island structures at the time shown in this figure are more concentrated near the left mouth, corresponding to the location where flux was entering the injector from the confinement volume prior to reversal. The right mouth on the other hand shows more complete reversal with larger scale island structures visible compared to the left mouth. This trend continues through the remainder of the reversal as island structures reconnect and dissipate, moving downstream (right to left in figure 5) along the flux being injected. The relationship of this progression, relative to the injector flux prior to reversal, holds for all reversal events following formation of a toroidal current. Prior to spheromak formation the reconnection process is more symmetric. If the toroidal current is reversed, the progression is also reversed. As the injector fields are strongly tied to the confinement volume during this period, as shown in figure 3, coupling may act to stabilize or destabilize the field more at one injector mouth. This would act to delay or trigger the reversal process leading to the observed asymmetry.

Field reversal is also visible as a deviation from the otherwise smooth injector flux coil current waveform required to reproduce sinusoidal injector flux. In figure 2 an increase in the time derivative of coil current is seen just proceeding reversal events in both the X ($t \approx \{1.34, 1.38, 1.41, 1.44\}$ ms) and Y ($t \approx \{1.36, 1.39, 1.43, 1.46\}$ ms) injectors. During and

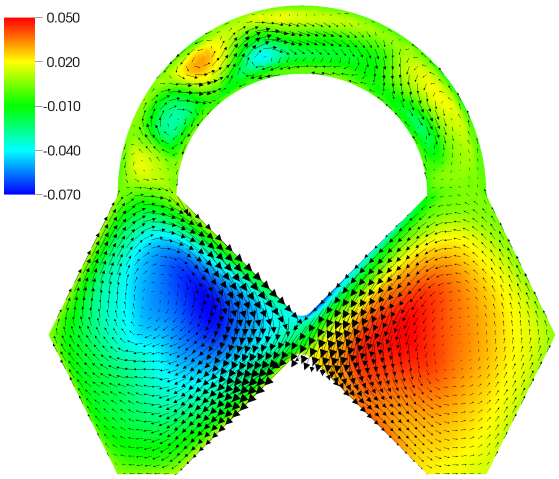

FIG. 5. Magnetic field in the X-Z plane from a PSI-TET simulation during field reversal in the X-injector (0.345 ms). In-plane field is shown as the black vectors while out-of-plane field strength is indicated by the shaded cross-section (scale in [T]).

following these field reversals a stagnation in flux coil current is observed. This stagnation in coil current, without a corresponding stagnation in the injector flux (loop voltage), indicates a large change in the inductance of the injector plasma during this time – consistent with a change in magnetic topology due to field reversal. Additionally, the flux coil currents show an asymmetry between the plasma response to flux injection in the two injectors. The coil currents on the X-Injector have a higher peak amplitude and exhibit a larger phase offset with respect to the flux waveform than the coil currents for the Y-Injector. These differences indicate that the plasma load on the X-Injector flux circuit is more dissipative than the Y-Injector in simulations. An asymmetry that is also observed experimentally during 14.5 kHz operation in HIT-SI. To further investigate this phenomenon a set of simulations were performed to determine the effect of injector phasing and toroidal current direction on the flux coil currents. Three additional simulations were performed and compared to the baseline case. The first simulation kept the same parameters and driver waveform as the base case, but changed the starting phase of all waveforms together to generate a negative toroidal current. For the other two simulations the relative phasing of the injectors was swapped so that the Y-Injector waveforms "led" the X-Injector. Starting phase was then varied to get one simulation each with positive and negative toroidal current. The observed

strength asymmetry was found to be dependent on phasing only, such that the higher amplitude waveform occurred when flux reversals corresponded to the two injectors switching from the same polarity (defined as the sign of driver waveform) to opposite polarities. This indicates that coupling between the injectors may be important in determining the relative loading on the driver coils.

To investigate a possible means of interaction between the two injectors, we employ the framework of force-free equilibria used extensively to study HIT-SI[4, 56, 62]. For these states, vacuum fields induced by circuits on different injectors are orthogonal to each other, resulting in no mutual coupling, but the injector fields do couple through common plasma modes in the confinement volume[56]. The coupling coefficients for each injector to the first 5 eigenmodes in HIT-SI are shown in table II. Coupling is computed as $\int_V \mathbf{B}_v^i \cdot \mathbf{B}_n dV$, where $\mathbf{B}_v^i$ is the vacuum field for injector i (with unit flux) and $\mathbf{B}_n$ is the n-th force-free eigenmode (with unit energy). In this force-free model the voltage and flux circuits are implicitly tied by the requirement of uniform parallel current density ($\lambda = \frac{\mathbf{j}\cdot\mathbf{B}}{B^2}$), therefore only the vacuum flux must be considered to compute mode coupling. The strongest couplings exist between the second and third modes, which share the odd symmetry of the injectors. Mode 3 represents the strongest interaction and couples the two injectors with matching polarities. Coupling of the injector fields through a common mode like this one may explain the asymmetry in coil current waveforms. During field reversals in the X-Injector, the existing flux will couple to the flux in the Y-Injector, which is ramping up, through this intermediate mode. This coupling may act to maintain the flux, requiring stronger drive, and thus coil currents, to reverse. For other reversal periods this effect would be present due to coupling through the second eigenmode, but weaker as observed. Non-linear coupling through a common third mode has also been observed experimentally for plasma modes that are linearly decoupled[63, 64]. Mutual coupling with the same polarity is also consistent with experimental observations of an "injector" mode. This "injector" mode manifests as a spontaneous offset of the injector flux and current that appears in both injectors with the same polarity.

TABLE II. Computed mode coupling for injector drive fields to force-free plasma eigenmodes in HIT-SI.

Eigenmode	X-Injector	Y-Injector
1	2.2×10^{-10}	-6.8×10^{-11}
2	-7.0×10^{-3}	9.6×10^{-3}
3	5.1×10^{-2}	5.1×10^{-2}
4	-2.1×10^{-10}	-1.4×10^{-10}
5	-4.2×10^{-11}	-3.8×10^{-11}

C. Drive Impedance

During high performance operation in HIT-SI, the impedance of the voltage coil circuits is well described by a real impedance, which scales linearly as the ratio j/n in the confinement volume[8]. This impedance is indicative of the underlying current drive mechanism that transfers magnetic energy from the injector driven region to the bulk plasma current. As a result, reproducing this impedance behavior is an important element in validating a model for studying helicity injection current drive in HIT-SI. Experimentally, the scaling is determined by comparing driver coil voltage and current waveforms in time with the toroidal current and line averaged electron density. However, with the present zero-β model plasma density is fixed in time, so impedance should only depend on the toroidal current. As the equivalent coil voltage is not readily available in simulations, a helicity balance model is used, where Ohmic dissipation from the spheromak equilibrium is assumed to be the dominant dissipation. As the injector flux and current are fixed the rate of helicity injection depends only on impedance. Helicity dissipation is due to resistive decay of the spheromak equilibrium with a characteristic time, $\tau_K = \frac{\mu_0}{2\eta\lambda^2}$, that is known from resistivity and $\lambda_{Taylor} = 10.3\ m^{-1}$. In steady state this gives the helicity balance in equation 5, where Z_{inj} is the voltage coil impedance, Ψ_{inj} is the quadrature injector flux, I_{inj} is the quadrature injector current, and $K \propto I_\phi^2$ is the normalized magnetic helicity associated with the toroidal current. By assuming balance this equation is only expected to hold when the toroidal current has reached steady-state.

$$Z_{inj}\Psi_{inj}I_{inj} = \frac{K}{\tau_K} \tag{5}$$

To investigate this scaling in simulations the background resistivity is scanned, with fixed plasma density and injector flux/current, to determine the dependence of the peak toroidal current on resistivity. If $Z_{inj} \propto j/n$ then the toroidal current should scale as $I_\phi \propto \eta^{-1}$. In general, if the impedance scales as $Z_{inj} \propto I_\phi^\alpha$ then toroidal current should scale as $I_\phi \propto \eta^{\frac{1}{\alpha-2}}$ with fixed plasma density and injector flux/current. Previous simulations without the injector volumes found a scaling of $I_\phi \propto \eta^{-0.6}$ ($Z_{inj} \propto I_\phi^{1/3}$), lower than the scaling expected from experimental observations. This process was repeated using PSI-TET by taking the baseline case and performing simulations at two additional resistivities ($\eta/\mu_0 = 12.5, 25$). The toroidal current evolution and saturated values for the three simulations used to determine scaling are shown in figure 6. These simulations show stronger scaling of toroidal current with resistivity of $I_\phi \propto \eta^{-0.86}$ ($Z_{inj} \propto I_\phi^{0.84}$). This impedance scaling agrees with experimental observations within the error determined in reference [8]. Scaling is slightly below the analytic prediction based on the Imposed Dynamo Current Drive (IDCD) model. However, simplifying approximations were required to derive both the analytic prediction and the helicity balance employed here. In particular variation in dissipation rates due to changes in the helicity content per unit current and decay time were not considered, which will be affected by evolution of the current profile that is expected to occur as the toroidal current grows.

The lowest resistivity, and highest current gain, simulation also sees the development of low frequency oscillations in the toroidal current late in time. These oscillations begin to manifest at a current gain of ≈ 3, which is within the operational range of HIT-SI at 14.5 kHz. Experimentally, oscillations like these cannot be distinguished from plasma circuit interaction that also tends to manifest as low frequency variation. Oscillations in the toroidal current have been seen in NIMROD simulations of HIT-SI with very low resistivity and high current amplification (≈ 6) where transient closed flux is formed[65]. However, Poincaré sections during this time in the PSI-TET with $\eta/\mu_0 = 12.5$ do not show any persistent flux surfaces. This phenomenon will be investigated further in comparison with higher frequency experimental operation, where high current amplification is seen.

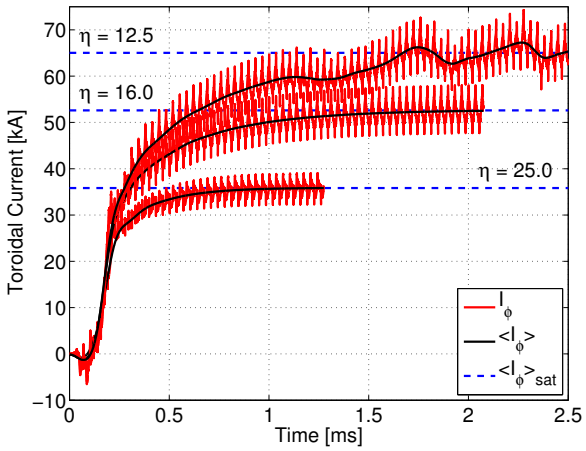

FIG. 6. Comparison of toroidal current (I_ϕ) evolution from simulations with different resistivities ($\eta/\mu_0 = 12.5, 16, 25$). Toroidal current following saturation is found to scale as $\eta^{-0.86}$, in good agreement with experimental observed impedance measurements[8].

V. COMPARISON TO EXPERIMENTAL DATA

In this section, we compare the baseline simulation with experimental data to assess the level of agreement in diagnostic signals. Before comparisons can be made the experimental and simulation timebases must be matched. For HIT-SI, this is done by first shifting the simulation timebase to match the time of toroidal current formation in both datasets. Then, the simulation is shifted by the smallest amount, either backward or forward in time, to match the injector current waveforms following current saturation ($\approx$ 1.5 ms) in the experimental data. For the baseline case presented here, the simulation was a shifted by 641.5 μs in time to provide the injector alignment shown in figure 8 and used for comparison to diagnostics. This shift produces good agreement with both experimental injector waveforms, which are not exactly 90 degrees out of phase with respect to each other as they are in the simulation. Figure 7 shows a comparison between the toroidal current in shot 122385 and the simulated toroidal current from the PSI-TET baseline simulation. Toroidal current for both the simulation and experiment is computed using discrete surface magnetic measurements to approximate Amperian loops[56]. The simulation reproduces the early formation time well, but the linear current growth observed in the experiment is not reproduced. This difference is primarily due to a corresponding ramp of the injector driving circuits in the

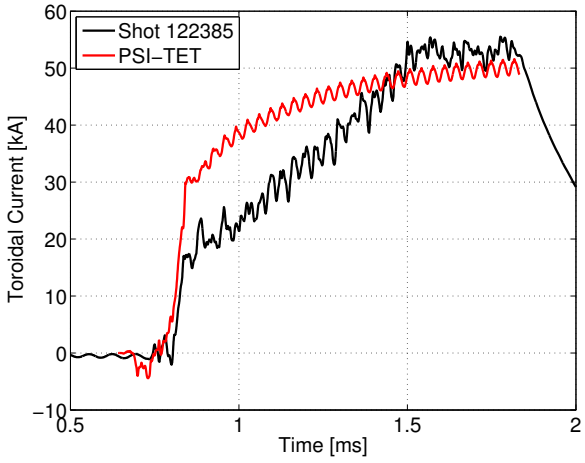

FIG. 7. Comparison of toroidal current (I_ϕ) from the PSI-TET baseline simulation to experimental data from shot 122385 at 14.5 kHz.

experiment over this time period, while the amplitude of the injectors is constant in the simulation. Injector waveforms that more closely match the experimental observed signals are being investigated for future validation simulations. Many of the comparisons presented here mirror those used in the previous validation study of zero-β Hall-MHD by Akcay[26]. For this paper we have limited comparisons to experimental data, with some comments on the differences to previous simulations. Detailed comparison between the two numerical models and experimental data for validation purposes will be presented in a separate paper to follow.

A. Comparison to Internal Magnetics

In HIT-SI profiles of the toroidal (B_ϕ) and poloidal (B_θ) magnetic field are measured along a radial chord by an internal magnetic probe. Evolution of these fields in experimental shot 122385 and simulation are compared in figure 9. In order to prevent clutter in the plot only a subset of probe locations are shown. The signals for each probe are also plotted with a fixed offset between locations of 50 mT and 80 mT for the poloidal and toroidal fields respectively. The major radius of each probe is given on the right side of each plot, just below the corresponding trace. The magnetic axis of the mean magnetic field in HIT-SI is located at ≈ 33 cm and the flux conserver is located at ≈ 55 cm.

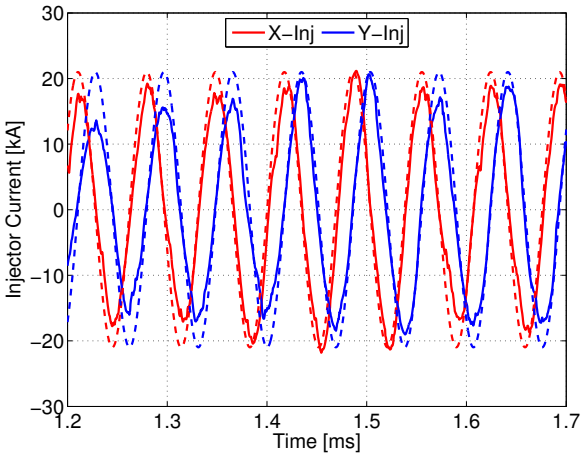

FIG. 8. Comparison of injector current waveforms from the PSI-TET baseline simulation (dashed) to experimental data from shot 122385 (solid) at 14.5 kHz.

Overall, good agreement is seen between PSI-TET and the experiment in both mean amplitude as well as the fluctuations from the injectors. The phase of injector driven oscillations agree well over the entire shot, with agreement in amplitude when experimental flux and current match the simulated values at approximately 1.5 ms. Significantly larger fluctuation amplitudes are produced early in time, before formation of a toroidal current, in the simulation despite good agreement in the formation time. This is likely due to lower experimental injector currents during this period. Following breakdown in the experiment a significant drop in the flux and current in the injectors is observed, resulting in decreased fluctuation amplitude. Fluctuations in the plasma density as well as its mean value are also higher during this period of time, indicating that density transport may have a stronger effect before relaxation. Similar oscillations, before relaxation, were also observed in previous simulations of HIT-SI[26].

Following relaxation, some small differences in fluctuation amplitude and character are seen in the poloidal field particularly near the mean field magnetic axis. The higher amplitude can be attributed to lower injector current in the experiment prior to 1.5 ms, as shown in figure 8. A difference is also present in time averaged values of both the toroidal and poloidal field when the toroidal currents are comparable, as with previous simulations[26]. This indicates a difference in the mean field equilibrium, which is important in validating the current drive mechanism[8], between simulations using zero-β MHD and the experiment

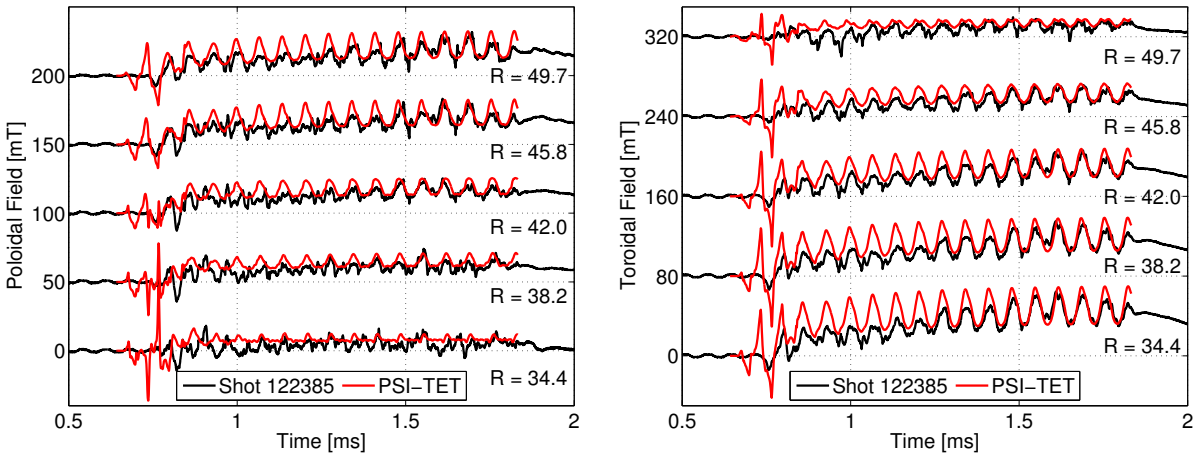

(a)Poloidal Field

(b)Toroidal Field

FIG. 9. Comparison of magnetic field evolution along the internal magnetic probe for the PSI-TET validation case and experimental data from shot 122385 at 14.5 kHz.

at 14.5 kHz. By restricting our system to uniform density and temperature, we are neglecting pressure forces as well as variation of plasma resistivity due to temperature, both of which can strongly impact the structure of equilibrium magnetic fields. Recent experimental observations[31] indicate that pressure effects are important in HIT-SI, at least with higher injector drive frequency. These effects will be addressed in future work using extended MHD models including plasma density and temperature dynamics that are available in both PSI-TET and NIMROD.

B. Comparison of Surface Magnetics Using Bi-Orthogonal Decomposition

Magnetic field is also measured on the interior surface of the flux conserver in HIT-SI using a distributed array of magnetic probes. Probes are arranged in 4 poloidal arrays of 16 probes each, placed at 0°, 45°, 180° and 225° toroidally, see figure 2 in reference [56]. As with the internal magnetic probe, toroidal and poloidal field are sampled at each location. Bi-Orthogonal Decomposition (BD)[66] is applied in order to compare coherent dynamics, from the 192 magnetic signals produced by this array, between experiment and simulations. The use of this method is motivated as the magnetic probes have a complicated (non-circular) spatial relationship that cannot be captured easily using Fourier methods. Additionally, BD has shown promise for the development of versatile, semi-automatic and quantitative metrics

for validating MHD models to experimental data[26]. BD is already used for analyzing experimental data from large diagnostic arrays[67, 68] and simulation results[69].

Bi-Orthogonal Decomposition is a method for decomposing groups of diagnostics signals into principal components for further analysis. In order to use this method the data must first be arranged into a signal matrix $Y_{i,j} = y_i(t_j)$, where individual diagnostic signals (y_i), sampled using the same time base, at discrete time points t_j, are stored as columns. This results in an $N \times M$ matrix where N is the number of diagnostic signals and M is the number of time points. The signal matrix is then decomposed using Singular Value Decomposition (SVD), equation 6, producing sets of singular values and vectors that correspond to the spatial and temporal dependence of principal modes[70] in the diagnostic signals. Each set is contained in one of the factored matrices, ϕ for the spatial vectors (topos), and Ψ for the temporal vectors (chronos). By convention these matrices are constructed to be unitary matrices, where the individual singular vectors are orthogonal to each other and have unit magnitude. Amplitudes (weights) for individual modes are stored in the diagonal matrix A. Modes are ordered such that mode amplitudes monotonically decrease, providing a heirarchy of structures beginning with the dominant (largest amplitude) mode. As the matrix Y is not square in general, only $K = MIN(N, M)$ modes exist with both spatial and temporal singular vectors. The remaining vector space in the larger dimension does not produce a mapping and can be neglected during analysis. For use in the following analysis a mode based notation will be used where the singular vectors and weights for the k-th mode are labeled as ϕ_k, $\mathbf{\Psi}_k$, and A_k.

$$Y = \phi A \Psi^T \tag{6}$$

For the comparisons presented here independent decomposition of signal matrices from experimental data (shot 122385) and the PSI-TET baseline simulation are performed. Comparisons are then made between amplitudes and shapes of modes within the resulting sets. To ensure consistent analysis simulation data was resampled on the experimental timebase (1 MHz), after shifting the data in time as described above. This ensures phase shifts and sampling differences do not affect the comparisons. The time window used for this analysis was 11 injector periods starting at 947 μs, to avoid known differences in the startup behavior described in section V A.

The resulting signal weight spectrum, A_k, for the first five modes from each of the decom-

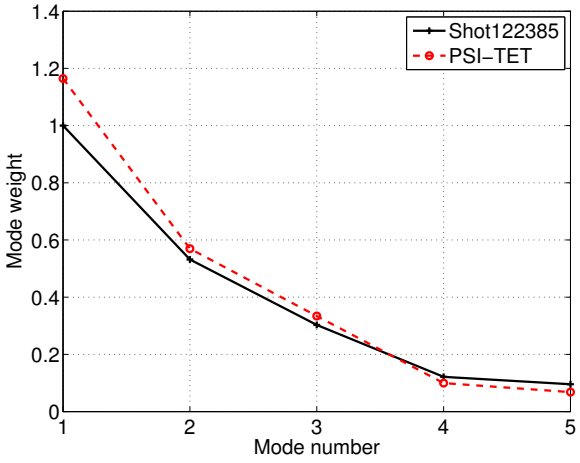

FIG. 10. Mode weights from independent BD analysis of surface magnetic probe signals from the PSI-TET validation case and experimental data from shot 122385 at 14.5 kHz.

positions are compared in figure 10. As magnetic signals are being used in the data matrix these amplitudes are directly related to the energy of each mode, integrated over the length of the sampling window, as $E_k \propto A_k^2 * M$. The qualitative shape of the mode spectrum is well reproduced in the PSI-TET simulation. Differences in the first and second mode amplitudes can be partially attributed to the difference in toroidal current evolution and injector amplitudes between experiment and simulation. From previous BD analysis of HIT-SI it is known that the first mode corresponds to the spheromak mean field state, while the second and third modes correspond primarily to the directly driven injector fluctuations. As a result these mode weights will be strongly influenced by the average value of the toroidal and injector currents. As the experimental injector current ramp in not captured in simulations, the average injector current over the sampled time period is higher in the simulation than experimentally. This injector current difference also contributes to the difference in toroidal current evolution, due to lower power injection at lower injector current.

Experimentally, the first BD mode has been found to accurately reproduce the measured toroidal current[31]. Therefore, we can use the scaled chrono ($A_1\Psi_1(t)$) for this mode to compare the temporal evolution of the toroidal current in simulation and experiment using a common calculation, figure 11. Using this method good agreement is seen between oscillations observed in the experiment and simulation. The source of discrepancy in the mode amplitudes for the first mode is also evident using this interpretation. Therefore, detailed

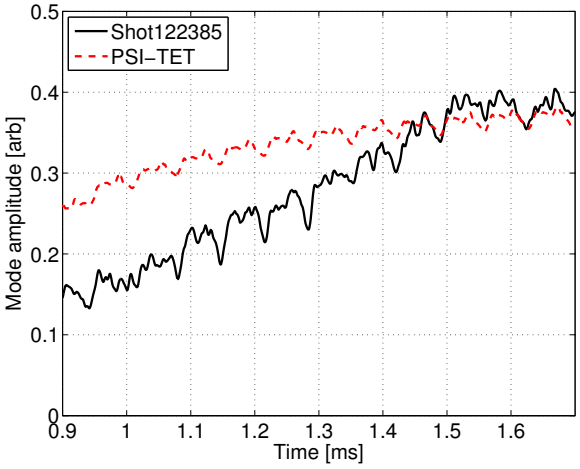

FIG. 11. Temporal behavior (chrono) of the first mode from independent BD analysis of surface magnetic probe signals from the PSI-TET validation case and experimental data from shot 122385 at 14.5 kHz.

comparison for validation will require matching the injector waveforms more closely.

To assess the agreement of topos between two data sets, Y^1 and Y^2, in a more quantitative manner, a correlation metric is defined, given by equation 7. Agreement for temporal behavior can be evaluated in the same manner. This metric quantifies agreement by measuring how well aligned the singular vectors are with respect to each other through the use of an inner product.

$$C_{i,j}^{1,2} = \phi_i^1 \cdot \phi_j^2 \tag{7}$$

As the individual singular vectors have unit magnitude this correlation will vary in the range $[0, 1]$ where 0 indicates the singular vectors are orthogonal, complete disagreement, and 1 indicates the singular vectors are identical, complete agreement.

This metric is used to analyze topos of the first 5 modes of the PSI-TET data set for correlation with the first five modes of the experimental data set in figure 12(a). Correlation is computed for each of the five modes in the simulation decomposition (colored bars) against the same modes from experimental decomposition (axis position). The same method is also used to compare chronos from the respective decompositions in figure 12(b). Good agreement (> 0.6) is seen with experiment in both spatial and temporal structures for the first four modes. The fourth mode was not well captured by previous simulations[26] – indicating injector geometry or coupling may be important for this mode. Analyzing the

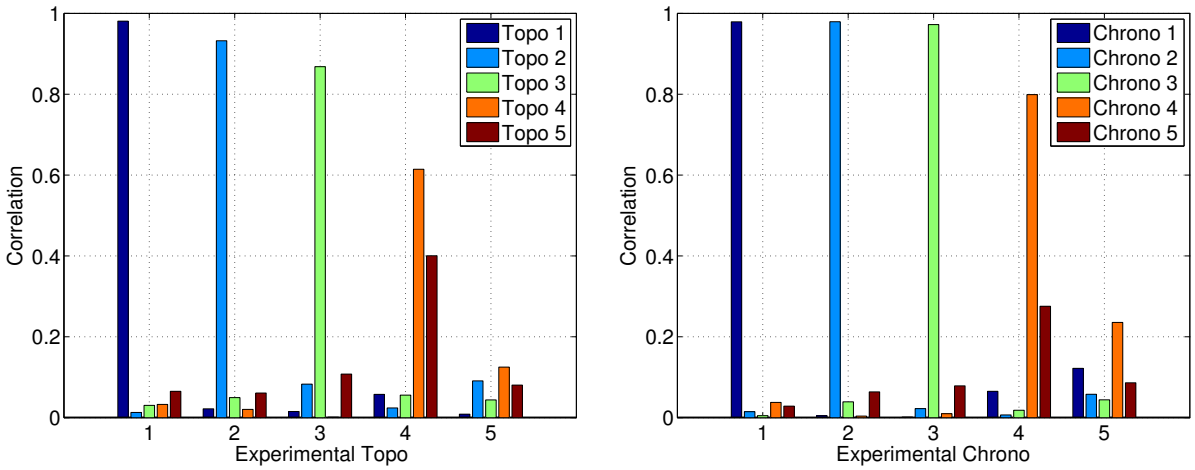

(a)Topo Correlations (b)Chrono Correlations

FIG. 12. Mode correlations between independent BD analyses of surface magnetic probe signals from the PSI-TET validation case and experimental data from shot 122385 at 14.5 kHz.

spatial structure shows a $n = 2$, $m = 1$ mode structure, where toroidal variation with $n = 2$ symmetry is seen near the X-injector and a more symmetric shape in the toroidal direction is seen near the Y-injector. The fourth mode's structure may be attributable to asymmetry introduced by the injector mouths on the nominally axisymmetric confinement volume. This effect is seen in the Taylor state for HIT-SI, which contains a large island at the $q = 1/2$ surface that is resonant with an $n = 2$, $m = 1$ structure, due to the perturbation induced by the injector mouths[35]. For the fifth mode, observed correlations are dominated by random low values (< 0.3) across many modes. This behavior is characteristic of correlations for higher modes as well, indicating poor correlation between experimental and simulation mode structure beyond the fourth mode. However, interpretation of agreement in these higher modes may be misleading as singular value decomposition is a non-linear process. Therefore, modes in the tail region, where mode energies are more closely spaced, are more susceptible to random mixing and reordering than higher amplitude modes. For this reason, only agreement in the first four modes, where the signal energy of each mode is greater than 10% of the total signal energy, are considered meaningful — with the fifth mode presented to illustrate the behavior of BD correlations for higher modes.

VI. CONCLUSION

This paper presents initial results for a new model that provides a more comprehensive tool for studying HIT-SI device than previously available. Initial simulations with this model have shown good agreement with experimental observations, while elucidating new dynamics associated with the helicity injectors. With the addition of injector regions, zero-β Hall-MHD also reproduces the experimentally observed injector impedance scaling with toroidal current. Simulations show significant asymmetry during the reversal processes, which appears to be due to coupling of injector drive fields to plasma modes in the confinement volume. Unfortunately, the helicity injectors are not well diagnosed in HIT-SI so direct comparison to experimental observations in these regions is not possible. However, observations of an "injector" mode in the experiment are consistent with the observed injector coupling in simulations.

As discussed in section V, many of the remaining differences observed between experiment and simulations may be attributable to differences in the drive waveforms. Detailed validation studies using PSI-TET and NIMROD, which capture variation in the injector amplitude, have been performed at 14.5 kHz to determine and quantify the remaining discrepancies[71]. These studies are extending simulations to different injector frequencies as well, where different performance and behavior has been observed experimentally[31]. Agreement with experimental observations at higher frequencies is expected to require plasma pressure and other dynamics. Further simulations with an extended MHD model capable of capturing these effects are now underway.

ACKNOWLEDGMENTS

The authors would like to thank the other members of the PSI-Center for many helpful discussions during the development of PSI-TET. Simulations presented here used resources of the National Energy Research Scientific Computing Center, which is supported by the U.S. Department of Energy Office of Science under Contract No. DE-AC02-05CH11231.

Work supported by USDoE.

---

[1] F. Najmabadi, A. Abdou, L. Bromberg, T. Brown, V. Chan, M. Chu, F. Dahlgren, L. El-Guebaly, P. Heitzenroeder, D. Henderson, H. S. John, C. Kessel, L. Lao, G. Longhurst, S. Malang, T. Mau, B. Merrill, R. Miller, E. Mogahed, R. Moore, T. Petrie, D. Petti, P. Politzer, A. Raffray, D. Steiner, I. Sviatoslavsky, P. Synder, G. Syaebler, A. Turnbull, M. Tillack, L. Waganer, X. Wang, P. West, and P. Wilson, Fusion Engineering and Design **80**, 3 (2006).

[2] G. Hoang, A. Bècoulet, J. Jacquinot, J. Artaud, Y. Bae, B. Beaumont, J. Belo, G. Berger-By, J. P. Bizarro, P. Bonoli, M. Cho, J. Decker, L. Delpech, A. Ekedahl, J. Garcia, G. Giruzzi, M. Goniche, C. Gormezano, D. Guilhem, J. Hillairet, F. Imbeaux, F. Kazarian, C. Kessel, S. Kim, J. Kwak, J. Jeong, J. Lister, X. Litaudon, R. Magne, S. Milora, F. Mirizzi, W. Namkung, J. Noterdaeme, S. Park, R. Parker, Y. Peysson, D. Rasmussen, P. Sharma, M. Schneider, E. Synakowski, A. Tanga, A. Tuccillo, and Y. Wan, Nuclear Fusion **49**, 075001 (2009).

[3] T. R. Jarboe, Fusion Science and Technology **36**, 85 (1999).

[4] T. R. Jarboe, W. T. Hamp, G. J. Marklin, B. A. Nelson, R. G. O'Neill, A. J. Redd, P. E. Sieck, R. J. Smith, and J. S. Wrobel, Phys. Rev. Lett. **97**, 115003 (2006).

[5] A. al Karkhy, P. K. Browning, G. Cunningham, S. J. Gee, and M. G. Rusbridge, Phys. Rev. Lett. **70**, 1814 (1993).

[6] D. J. Den Hartog, J. T. Chapman, D. Craig, G. Fiksel, P. W. Fontana, S. C. Prager, and J. S. Sarff, Physics of Plasmas (1994-present) **6**, 1813 (1999).

[7] W. X. Ding, D. L. Brower, D. Craig, B. H. Deng, G. Fiksel, V. Mirnov, S. C. Prager, J. S. Sarff, and V. Svidzinski, Phys. Rev. Lett. **93**, 045002 (2004).

[8] T. Jarboe, B. Victor, B. Nelson, C. Hansen, C. Akcay, D. Ennis, N. Hicks, A. Hossack, G. Marklin, and R. Smith, Nuclear Fusion **52**, 083017 (2012).

[9] J. B. Taylor, Phys. Rev. Lett. **33**, 1139 (1974).

[10] T. R. Jarboe, I. Henins, A. R. Sherwood, C. W. Barnes, and H. W. Hoida, Phys. Rev. Lett. **51**, 39 (1983).

[11] E. Hooper, L. Pearlstein, and R. Bulmer, Nuclear Fusion **39**, 863 (1999).

[12] R. Wood, D. Hill, E. Hooper, S. Woodruff, H. McLean, and B. Stallard, Nuclear Fusion **45**, 1582 (2005).

[13] A. J. Redd, B. A. Nelson, T. R. Jarboe, P. Gu, R. Raman, R. J. Smith, and K. J. McCollam, Physics of Plasmas (1994-present) **9**, 2006 (2002).

[14] B. Nelson, T. Jarboe, D. Mueller, R. Raman, M. Bell, J. Menard, M. Ono, A. Roquemore, V. Soukhanovskii, H. Yuh, and the NSTX Research Team, Nuclear Fusion **51**, 063008 (2011).

[15] K. J. McCollam, J. K. Anderson, A. P. Blair, D. Craig, D. J. Den Hartog, F. Ebrahimi, R. O'Connell, J. A. Reusch, J. S. Sarff, H. D. Stephens, D. R. Stone, D. L. Brower, B. H. Deng, and W. X. Ding, Physics of Plasmas (1994-present) **17**, 082506 (2010).

[16] B. I. Cohen, E. B. Hooper, R. H. Cohen, D. N. Hill, H. S. McLean, R. D. Wood, S. Woodruff, C. R. Sovinec, and G. A. Cone, Physics of Plasmas (1994-present) **12**, 056106 (2005).

[17] E. B. Hooper, B. I. Cohen, H. S. McLean, R. D. Wood, C. A. Romero-Talamas, and C. R. Sovinec, Physics of Plasmas **15**, 032502 (2008).

[18] F. Ebrahimi, E. B. Hooper, C. R. Sovinec, and R. Raman, Physics of Plasmas (1994-present) **20**, 090702 (2013).

[19] J. B. O'Bryan, C. R. Sovinec, and T. M. Bird, Physics of Plasmas (1994-present) **19**, 080701 (2012).

[20] F. Ebrahimi, S. C. Prager, J. S. Sarff, and J. C. Wright, Physics of Plasmas (1994-present) **10**, 999 (2003).

[21] T. Gray, V. S. Lukin, M. R. Brown, and C. D. Cothran, Physics of Plasmas (1994-present) **17**, 102106 (2010).

[22] N. Oreskes, K. Shrader-Frechette, and K. Belitz, Science **263**, 641 (1994).

[23] F. Stern, R. V. Wilson, H. W. Coleman, and E. G. Paterson, Journal of Fluids Engineering **123**, 793 (2001).

[24] M. Greenwald, Physics of Plasmas (1994-present) **17**, 058101 (2010).

[25] M. J. Lanctot, H. Reimerdes, A. M. Garofalo, M. S. Chu, Y. Q. Liu, E. J. Strait, G. L. Jackson, R. J. La Haye, M. Okabayashi, T. H. Osborne, and M. J. Schaffer, Physics of Plasmas (1994-present) **17**, 030701 (2010).

[26] C. Akcay, C. C. Kim, B. S. Victor, and T. R. Jarboe, Physics of Plasmas **20**, 082512 (2013).

[27] T. Jarboe, C. Akcay, M. Chilenski, D. Ennis, C. Hansen, N. Hicks, R. A. Hosn, A. Hossack, G. Marklin, B. Nelson, R. O'Neill, P. Sieck, R. Smith, B. Victor, J. Wrobel, and M. Nagata,

Nuclear Fusion **51**, 063029 (2011).

[28] B. S. Victor, T. R. Jarboe, A. C. Hossack, D. A. Ennis, B. A. Nelson, R. J. Smith, C. Akcay, C. J. Hansen, G. J. Marklin, N. K. Hicks, and J. S. Wrobel, Phys. Rev. Lett. **107**, 165005 (2011).

[29] M. Rosenbluth and M. Bussac, Nuclear Fusion **19**, 489 (1979).

[30] T. R. Jarboe, Plasma Physics and Controlled Fusion **36**, 945 (1994).

[31] B. S. Victor, T. R. Jarboe, C. J. Hansen, C. Akcay, K. D. Morgan, A. C. Hossack, and B. A. Nelson, Physics of Plasmas (1994-present) **21**, 082504 (2014).

[32] V. A. Izzo and T. R. Jarboe, Physics of Plasmas **12**, 056109 (2005).

[33] C. Sovinec, A. Glasser, T. Gianakon, D. Barnes, R. Nebel, S. Kruger, D. Schnack, S. Plimpton, A. Tarditi, and M. Chu, Journal of Computational Physics **195**, 355 (2004).

[34] D. D. Schnack, D. C. Barnes, D. P. Brennan, C. C. Hegna, E. Held, C. C. Kim, S. E. Kruger, A. Y. Pankin, and C. R. Sovinec, Physics of Plasmas **13**, 056110 (2006).

[35] C. Hansen, PhD Dissertation, University of Washington (2014).

[36] CUBIT Development Team, "Cubit: Geometry and mesh generation toolkit," (2013).

[37] D. Rypl, "T3D Mesh Generator," (2004), Department of Mathematics, Czech Technical University.

[38] J. Nedelec, Numerische Mathematik **35**, 315 (1980).

[39] J. Schöberl and S. Zaglmayr, COMPEL: The International Journal for Computation and Mathematics in Electrical and Electronic Engineering **24**, 374 (2005).

[40] T. M. Forum, "MPI: A Message Passing Interface," (1993).

[41] OpenMP Architecture Review Board, "OpenMP Application Program Interface Version 3.1," (2011).

[42] G. Karypis and V. Kumar, SIAM J. Sci. Comput. **20**, 359 (1998).

[43] S. Balay, J. Brown, K. Buschelman, W. D. Gropp, D. Kaushik, M. G. Knepley, L. C. McInnes, B. F. Smith, and H. Zhang, "PETSc Web page," (2012), http://www.mcs.anl.gov/petsc.

[44] R. Hiptmair, SIAM Journal on Numerical Analysis **36**, 204 (1998).

[45] K. Stüben, Journal of Computational and Applied Mathematics **128**, 281 (2001).

[46] L. Chacón, D. Knoll, and J. Finn, Journal of Computational Physics **178**, 15 (2002).

[47] R. S. Sampath and G. Biros, SIAM Journal on Scientific Computing **32**, 1361 (2010).

[48] R. Graglia, D. Wilton, and A. Peterson, Antennas and Propagation, IEEE Transactions on

45, 329 (1997).

[49] J. Webb, Antennas and Propagation, IEEE Transactions on **47**, 1244 (1999).

[50] A. Schneebeli and D. Schötzau, Comptes Rendus Mathematique **337**, 71 (2003).

[51] C. Greif, D. Li, D. Schötzau, and X. Wei, Computer Methods in Applied Mechanics and Engineering **199**, 2840 (2010).

[52] Y. Saad, SIAM Journal on Scientific Computing **14**, 461 (1993).

[53] J. W. Demmel, S. C. Eisenstat, J. R. Gilbert, X. S. Li, and J. W. H. Liu, SIAM J. Matrix Analysis and Applications **20**, 720 (1999).

[54] L. Spitzer, *Physics of fully ionized gases* (Interscience Publishers, 1962).

[55] S. I. Braginskii, Reviews of Plasma Physics **1**, 205 (1965).

[56] J. S. Wrobel, C. J. Hansen, T. R. Jarboe, R. J. Smith, A. C. Hossack, B. A. Nelson, G. J. Marklin, D. A. Ennis, C. Akcay, and B. S. Victor, Physics of Plasmas **20**, 012503 (2013).

[57] A. Bondeson, G. Marklin, Z. G. An, H. H. Chen, Y. C. Lee, and C. S. Liu, Physics of Fluids (1958-1988) **24**, 1682 (1981).

[58] U. Shumlak and T. Jarboe, Physics Of Plasmas **7**, 2959 (2000).

[59] P. A. Sweet, in *Electromagnetic Phenomena in Cosmical Physics*, IAU Symposium, Vol. 6, edited by B. Lehnert (1958) p. 123.

[60] E. N. Parker, Journal of Geophysical Research **62**, 509 (1957).

[61] S. Donato, S. Servidio, P. Dmitruk, V. Carbone, M. A. Shay, P. A. Cassak, and W. H. Matthaeus, Physics of Plasmas **19**, 092307 (2012).

[62] R. G. O'Neill, G. J. Marklin, T. R. Jarboe, C. Akcay, W. T. Hamp, B. A. Nelson, A. J. Redd, R. J. Smith, B. T. Stewart, J. S. Wrobel, and P. E. Sieck, Physics of Plasmas (1994-present) **14**, 112304 (2007).

[63] S. Assadi, S. C. Prager, and K. L. Sidikman, Phys. Rev. Lett. **69**, 281 (1992).

[64] C. C. Hegna, Physics of Plasmas (1994-present) **3**, 4646 (1996).

[65] C. Akcay, PhD Dissertation, University of Washington (2013).

[66] T. Dudok de Wit, A. Pecquet, J. Vallet, and R. Lima, Physics of Plasmas **1**, 3288 (1994).

[67] C. Nardone, Plasma Physics and Controlled Fusion **34**, 1447 (1992).

[68] J. Levesque, N. Rath, D. Shiraki, S. Angelini, J. Bialek, P. Byrne, B. DeBono, P. Hughes, M. Mauel, G. Navratil, Q. Peng, D. Rhodes, and C. Stoafer, Nuclear Fusion **53**, 073037 (2013).

[69] B. R. Noack, K. Afanasiev, M. Morzynski, G. Tadmor, and F. Thiele, Journal of Fluid Mechanics **497**, 335 (2003).

[70] K. Pearson, Philosophical Magazine Series 6 **2**, 559 (1901).

[71] C. Hansen, B. Victor, K. Morgan, T. Jarboe, A. Hossack, G. Marklin, B. A. Nelson, and D. Sutherland, Physics of Plasmas (1994-present) **22**, 056105 (2015), http://dx.doi.org/10.1063/1.4919277.